Meteoritics & Planetary Science 41, Nr 9, 1361–1379 (2006)
Abstract available online at http://meteoritics.org

Major and trace element compositions of melt particles and associated phases from the Yaxcopoil-1 drill core, Chicxulub impact structure, Mexico

Martin G. TUCHSCHERER[1, 2*], W. Uwe REIMOLD[1, 3], Roger L. GIBSON[1], Deon DE BRUIN[4], and Andreas SPÄTH[5]

[1]Impact Cratering Research Group, School of Geosciences, University of the Witwatersrand, Private Bag 3, P.O. Wits, 2050, Johannesburg, South Africa
[2]Caracle Creek International Consulting Inc., Postnet Suite 81, Private Bag X9, Melville, 2109, South Africa
[3]Museum für Naturkunde, Humboldt-Universität, Invalidenstrasse 43, D-10115 Berlin, Germany
[4]Council for Geoscience, Private Bag X112, 0001 Pretoria, South Africa
[5]Department of Geological Sciences, University of Cape Town, Rondebosch, 7701, South Africa
*Corresponding author. E-mail: tuchscm@gmail.com

(Received 15 November 2005; revision accepted 26 June 2006)

Tables 3–5 for this article are available online at http://meteoritics.org.

Abstract–Melt particles found at various depths in impactites from the Yaxcopoil-1 borehole into the Chicxulub impact structure (Yucatán) have been analyzed for their major and trace element abundances. A total of 176 electron microprobe and 45 LA-ICP-MS analyses from eight different melt particles were investigated. The main purpose of this work was to constrain the compositions of precursor materials and secondary alteration characteristics of these melt particles. Individual melt particles are highly heterogeneous, which makes compositional categorization extremely difficult. Melt particles from the uppermost part of the impactite sequence are Ca- and Na-depleted and show negative Ce anomalies, which is likely a result of seawater interaction. Various compositional groupings of melt particles are determined with ternary and binary element ratio plots involving major and trace elements. This helps distinguish the degree of alteration versus primary heterogeneity of melt phases. Comparison of the trace element ratios Sc/Zr, Y/Zr, Ba/Zr, Ba/Rb, and Sr/Rb with compositions of known target rocks provides some constraints on protolith compositions; however, the melt compositions analyzed exceed the known compositional diversity of possible target rocks. Normalized REE patterns are unique for each melt particle, likely reflecting precursor mineral or rock compositions. The various discrimination techniques indicate that the highly variable compositions are the products of melting of individual minerals or of mixtures of several minerals. Small, angular shards that are particularly abundant in units 2 and 3 represent rapidly quenched melts, whereas larger particles (>0.5 mm) that contain microlites and have fluidal, schlieric textures cooled over a protracted period. Angular, shard-like particles with microlites in unit 5 likely crystallized below the glass transition temperature or underwent fragmentation during or after deposition.

INTRODUCTION

In 2002, the International Continental Scientific Drilling Program (ICDP) retrieved the Yaxcopoil-1 (Yax-1) drill core about 60 km south-southwest of the center of the Chicxulub impact structure (Fig. 1) (Dressler et al. 2003). This project was carried out because the retrieval and study of impactites from the Chicxulub impact structure was considered of prime scientific importance regarding a plethora of aspects involving impact cratering processes. The Yax-1 core provides a complete crater fill intersection, including a thick layer of impact melt rock. The melt rock particles at Chicxulub are believed to be the vitrification product of bulk rock and/or mineral melts. However, no adequate constraints that would allow a determination of the degree of melting and mixing in Chicxulub melt rock particles have yet been obtained. Impact melts are produced under extreme temperatures and pressures that are not typical for traditional endogenic processes (e.g., Melosh 1989; French 1998). Thus, the study of impact melt rock particles provides valuable

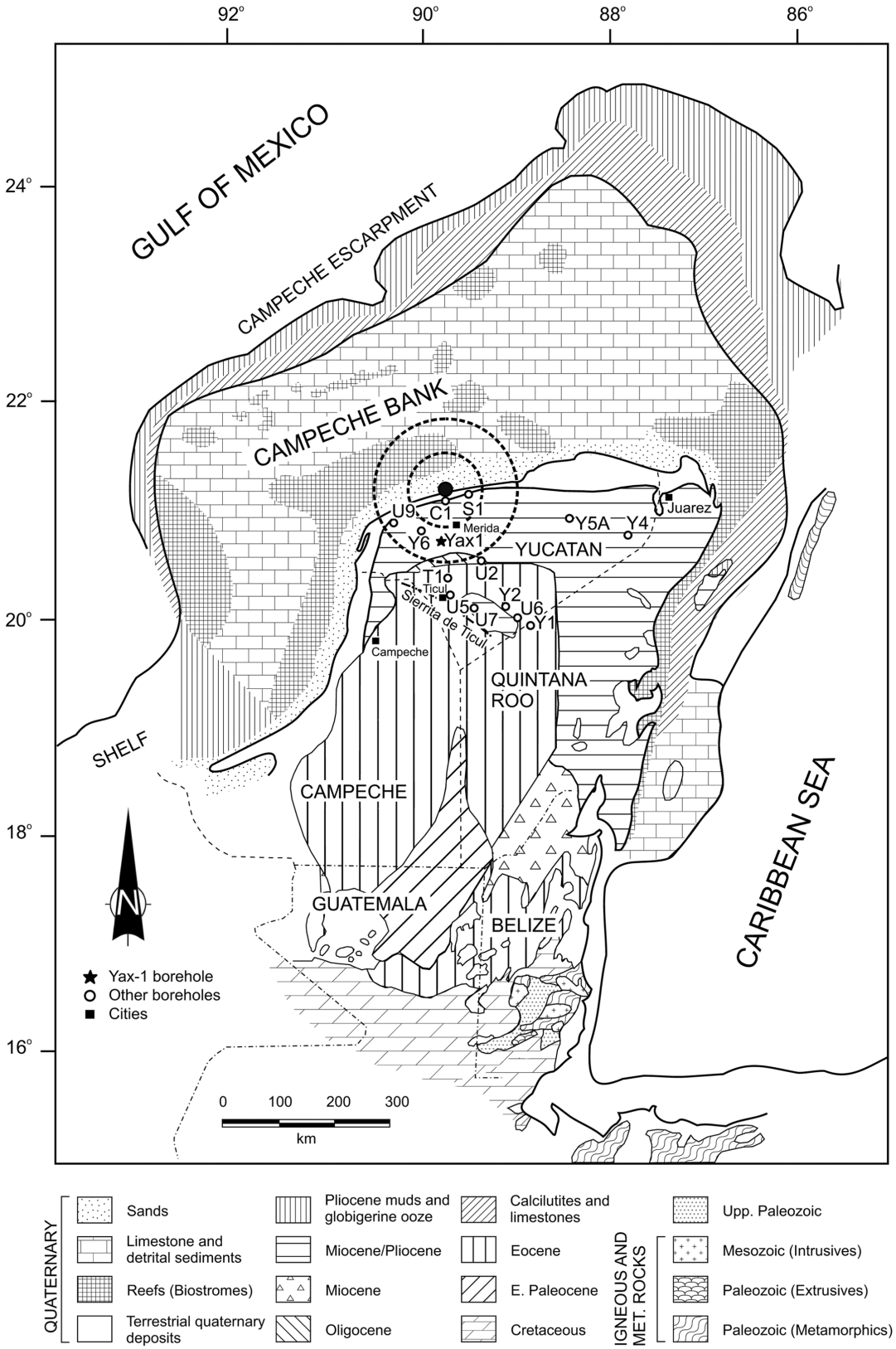

Fig. 1. The surface and offshore geology of the Yucatán Peninsula of Mexico with the location of the Chicxulub impact structure, as well as the Yaxcopoil-1 (Yax-1) and other boreholes (modified after Lopez-Ramos 1975). Note that the nearest exposures of Cretaceous target rocks occur in Belize and Guatemala, several hundred kilometers from the impact structure.

information about cratering dynamics (e.g., Dressler 1996; Hörz et al. 2002). Impact melt particles are commonly found as part of either fallback deposits in impact structures, fallout deposits of impact breccia, and even as clasts in injection dikes within the crater floor (Dressler and Reimold 2001).

The Yax-1 drill core recovered 100 m of continuous impactites between 795 and 895 m depth. Dressler et al. (2003) recognized six stratigraphic subdivisions, which have since been adopted by many Yaxcopoil-1 researchers. Our group, in contrast, has only recognized five subdivisions (Tuchscherer et al. 2004a, 2004b), as we prefer to combine the upper two units of Dressler et al. (2003) into one unit (compare stratigraphic column of Fig. 2). Initial petrographic and geochemical information about the impactites and their stratigraphy has been published in two special Yax-1 issues of *Meteoritics & Planetary Science* (volume 39, issues 6 and 7; in particular, the contributions by Ames et al. 2004; Dressler et al. 2004; Hecht et al. 2004; Kring et al. 2004; Schmitt et al. 2004; Stöffler et al. 2004; Tuchscherer et al. 2004a, 2004b, 2005; Wittmann et al. 2004; Zurcher et al. 2004). In the Yax-1 core, the retrieved impactites are believed to represent a depositional sequence of ejecta, massive melt rock, and a sequence of fallback suevite that have been preserved in the outer part of the impact structure (Stöffler et al. 2004; Tuchscherer et al. 2004a, 2004b, 2005). The uppermost unit of suevitic breccia is believed to have been reworked by the resurge of seawater (suevite is defined as a clastic matrix, melt-particle-bearing impactite—e.g., Dressler and Reimold 2001).

Previous studies on Yax-1 melt rock particle compositions, mostly obtained by EMPA, were reported by Ames et al. (2004), Dressler et al. (2004), Hecht et al. (2004), Kring et al. (2004), Tuchscherer et al. (2004a), and Zurcher et al. (2004). They showed that the impactites are compositionally heterogeneous, which was attributed to incomplete mixing of compositionally diverse target rocks in the formation of melts, dilution with a large secondary carbonate component, and hydrothermal as well as seawater alteration that converted silicate phases into phyllosilicates. Ames et al. (2004) and others showed that a great proportion of melt rock particles had been converted to phyllosilicate phases, as a result of low-temperature seawater alteration. Dressler et al. (2004) concluded that melt particle compositions were generally homogeneous when recalculated on a L.O.I. free basis. They found a bimodal compositional distribution that they attributed to the melting and mixing of felsic/intermediate and mafic silicate target rocks. Hecht et al. (2004) recognized four types of melt particles based on petrographic characteristics, i.e., the degree of crystallization, color, shape, vesiculation, and clast content. Three types of alteration phases (sm1, sm2, and sm3) were also identified. Tuchscherer et al. (2004a) distinguished three types of melt particles (1 = mafic, 2 = mafic-alkali element-rich, and 3 = alkali element-rich) that all registered a K overprint. All mafic particles are thoroughly altered, whereas

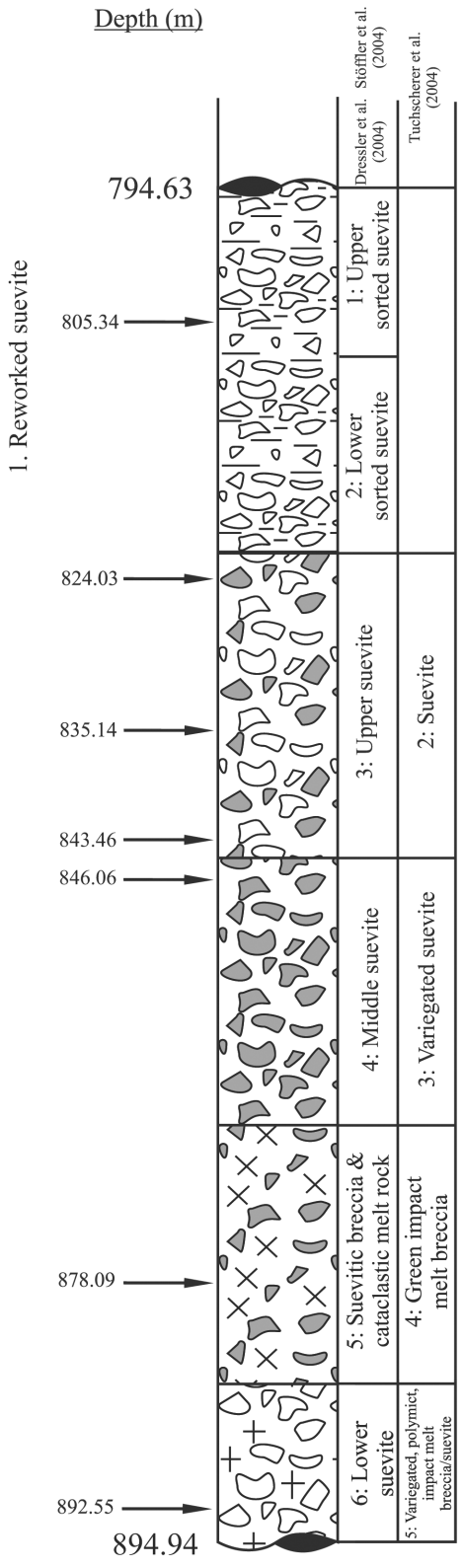

Fig. 2. Stratigraphy of the continuous impactite sequence retrieved from the Yax-1 borehole; sample depths are indicated as well. The stratigraphy of Dressler et al. (2004) and Stöffler et al. (2004) is shown for comparison.

the more felsic particles analyzed commonly yield analytical totals near 100 wt%. Tuchscherer et al. (2004b) also analyzed bulk impact melt rock samples and noted that the green impact melt rock of unit 4 (Fig. 2) has a composition involving a significant mafic component. Brown melt particles show similar compositions but a higher CaO content. Tuchscherer et al. (2005) analyzed melt particles for trace element abundances and found that they represent mixtures of known target rocks (clastic supracrustals, granitic gneiss, granodiorite) with a mafic component (possibly amphibolite, as reported by Kettrup and Deutsch 2003).

For this contribution, we obtained major and trace element compositions for selected melt rock particles from different units of the Yax-1 core by electron microprobe (EMP) and laser-ablation-inductively coupled plasma-mass spectrometry (LA-ICP-MS). The results allow us to comment on the extent of melting involved during melt particle generation (mineral melting, bulk rock melting), mixing dynamics, cooling rates, and the effects of secondary alteration processes.

GEOLOGY

The Chicxulub impact structure is centered on the northwestern region of the Yucatán Peninsula (Fig. 1), which has a poorly known subsurface regional geology. The best geological compilation for the area was given by Lopez Ramos (1975). Geological observations at surface show that Tertiary and Quaternary rocks overlie the Chicxulub structure. Offshore rocks comprise Quaternary limestone with extensive biostromes. The nearest surface exposure of Cretaceous and Upper Paleozoic sedimentary/crystalline target rocks is found to the south of the Yucatán Peninsula, in Belize and Guatemala, where Chicxulub ejecta also occur (e.g., Pope et al. 2005). These deposits also provide insight into the composition of the Yucatán basement: the distal fallout breccias are generally carbonate-rich; clasts are composed of micritic and coarse crystalline limestone, laminated dolomite, and calcareous mudstone. Detailed studies on buried ejecta deposits sampled by the UNAM 5-7 boreholes located closer toward the crater center show a proportion of silicate clasts progressively increasing toward the crater center (e.g., Sharpton et al. 1999). Other fallout deposits in northeast Mexico contain melt spherules that are mafic to intermediate in composition, which likely reflects compositionally varied target rocks (Schulte and Kontny 2005). Zircons sampled in K/T boundary ejecta from the Raton basin of Colorado and Saskatchewan indicate Pan-African ages (544 ± 5, 548 ± 6 Myr) (Kamo and Krogh 1995) for the crystalline basement in the Chicxulub target region. Various lithic clasts were observed in the impactites of the Yax-1 borehole. Sedimentary rocks comprise limestone, dolomite, quartzite grains, and argillaceous limestone. Rocks from the silicate basement consist of granite, gabbronorite, gneiss, and schist (Tuchscherer et al. 2004a, 2005).

METHODOLOGY

Polished sections ~150 μm in thickness were prepared from samples from 805.34, 824.03, 835.14, 843.46, 846.06, 878.09, and 892.55 m depths (Fig. 2). These "thick sections" were investigated with a petrographic microscope and a scanning electron microscope (SEM) to describe the various melt particles present. Once melt particle characteristics of a given unit had been identified, a backscattered electron (BSE) study was undertaken in preparation of quantitative EMPA and LA-ICP-MS work. Backscattered electron imaging was done at the Council for Geoscience, Pretoria, with a Leica 440 Stereoscan instrument with a LINK OXFORD energy-dispersive X-ray analysis system, at 20 kV, 2 nA, and 25 mm working distance. Quantitative electron microprobe analyses were collected for the elements Si, Ti, Al, Cr, Fe, Mn, Mg, Ca, and Na in wavelength-dispersive mode on a JEOL 733 Superprobe, at 15 kV, 20 nA, and 39 mm working distance, also at the Council for Geoscience. The width of the electron beam was 3 μm; peak counting times were 10 s with 5 s counting times on symmetrical background positions. The standard K-H (USNM 143965) (Jarosewich et al. 1980) was used for SiO_2, Al_2O_3, FeO_{tot}, CaO, Na_2O, and K_2O analysis, synthetic rutile for TiO_2, natural rhodonite for MnO, and the chromite standard USNM 117075 for Cr_2O_3 standardization. Data reduction was done with the JEOL Fortran program FZAFOC.

The concentrations of 26 trace elements (Sc, Ti, V, Cr, Ni, Co, Rb, Sr, Y, Zr, Nb, Ba, La, Ce, Pr, Nd, Sm, Eu, Tb, Gd, Dy, Ho, Er, Tm, Yb, and Lu) were determined by LA-ICP-MS at the University of Cape Town (UCT) in particles previously analyzed by EMP. The UCT instrument is a Perkin Elmer ELAN6000 ICP-MS equipped with a CETAC LSX-200 laser ablation module. The frequency quadrupled Nd-YAG laser produces radiation with a wavelength of 266 nm and was operated at an energy level of approximately 5 mJ per pulse and at a frequency of 5 Hz. Ablation pits 100 μm in diameter were excavated. Each analysis comprised the acquisition of three replicate analyses from 85 sweeps each across the selected mass range, at dwell times of 10 μs per mass peak. Calibration was done by hourly external standardization of all trace elements using the NIST 610 and 612 glass standards with background limits obtained by analysis of the carrier argon gas. Internal standardization was used to correct for instrument drift and differences in ablation yield from spot to spot. Calcium was used as an internal standard, based on Ca concentration results from EMPA. Off-line computer software (such as GLITTER) was not used to reprocess the data. Oxide levels were minimized by ensuring that Th/ThO was <0.005 during daily instrument optimization. Isobaric interference corrections based on the knowledge of naturally occurring isotope abundances (e.g., ^{144}Sm on ^{144}Nd) were made automatically by the instrument software. Typical precision and accuracy values for such analyses range from 1 to 10%

Table 1. Petrographic characteristics and abundances (from Tuchscherer et al. 2004a) of melt rock particles found in the various impactite units of the Yax-1 borehole.

Unit	1	2	3	4	5
Abundance	63 vol%	62 vol%	66 vol%	94 vol%	33 vol%
Shape	Rounded to subangular	Subrounded to subangular	Subrounded to subangular	Subangular to angular	Subrounded to subangular
Schlieren	No	No	Yes, common	Yes, occasional	Yes, occasional
Hand sample color	Mostly green	Mostly green	Variegated, green, beige, brown, red	Mostly green with yellow, brown, and green tinges	Variegated, green, beige, brown
Microscopic color	Yellow to brown green (altered)	Yellowish green	Dark to medium brown red and gray	Green gray	Yellow gray
Perlitic fractures	Yes	Rare	No	No	No
Vesicles	Yes	Yes	Yes	No	No
Microlites	No	Yes	Yes	Yes	Yes
Inclusions[a]	Cc, qtz, fs	Cc, qtz, fs	Cc, qtz, fs, ap	Qtz, fs, bio	Cc, qtz

[a]Abbreviations: cc = Calcite, qtz = quartz, fs = feldspar, bio = biotite, ap = apatite.

Table 2. General description of melt particle material analyzed by EMPA and LA-ICP-MS for this study.

Thin section depth (m)	Unit	Type of melt particle material analyzed
805.34	1	Reworked green melt particle with secondary calcite intergrowths replacing altered mesostasis
824.03	2	Small, altered green, vesiculated melt shard with no microlites
835.14	2	Altered, subrounded, gray melt particle with detrital quartz inclusions and other noticeable compositional heterogeneities
843.46	2	Altered brown melt particle with quartz clast and microlites
846.06	3	Two altered, zoned, beige melt particles with microlites
878.09	4	Altered crystalline patch overprinting melt particle and microlite-bearing melt particle
892.55	5	Traverse through a melt shard with microlites

(Grégoire et al. 2002). Repeat analysis of a UCT in-house glass standard (V40-56) produced 2σ error variations of <5% for Sc, Ni, Rb, Sr, Y, Zr, Nb, Ba, the rare earth elements (REE), Th, and U. For this instrument, Le Roux et al. (2002) indicated lower limits of detection (LLD) for all elements at less than 0.2 ppm, except for Ni (<1 ppm), and Sc and Ba (<0.4 ppm). Theoretical LLD ranges from 10 to 20 ppb were predicted for the REE, Ba, Rb, Nb, Sr, Zr, and Y, to 100 ppb for V and Sc, and to 2 ppm for Ti, Ni, and Cr (Grégoire et al. 2002). Le Roux et al. (2002) determined (for ablation craters 100 μm in diameter) the LLD for these major and trace elements at: Sc (0.36), Ni (1.06), Rb (0.12), Sr (0.08), Y (0.07), Zr (0.19), Nb (0.11), Ba (0.41), La (0.08), Ce (0.06), Nd (0.23), Sm (0.19), Eu (0.08), Gd (0.21), Dy (0.19), Er (0.14), Yb (0.13) (all values in ppm). LLD for the other trace elements were published by Potts et al. (1995), for an LA-ICP-MS operating at 7 Hz, at 100 sweeps, 320 μs dwell time, and ablation pits of 150 μm: Ti (0.03), V (0.06), Cr (0.30), Co (0.08), Pr (0.02), Tb (0.009), Ho (0.007), Tm (0.009), Lu (0.02) (values in ppm).

SAMPLES STUDIED

Table 1 summarizes the petrographic characteristics of the selected melt particles and their overall modal abundances in the various units. As discussed, the melt particles throughout the impactite sequence all register variable degrees of alteration (Ames et al. 2004; Hecht et al. 2004; Tuchscherer et al. 2004a; and Zurcher et al. 2004). More petrographic detail about these melt particles is provided in Table 2 and in the following unit description sections. Figure 3 shows backscattered electron (BSE) images of these melt particles, with analytical traverses and LA-ICP-MS spots also shown.

Unit 1

From this unit, a sample from 805.34 m depth was selected for analysis (Fig. 3a). It is a reworked suevite that comprises an amalgamated mass of highly altered and fractured melt particles. No significant groundmass material is observed macroscopically, owing to the compacted nature of the melt particles. Highly altered lithic clasts (gneiss, carbonate, and monomineralic quartz) are present. The melt particle boundaries are irregular. Fracturing is strong, and, accordingly, the sample is highly friable. The analyzed melt particle region is characterized by well-preserved, often circular cross-sections of vesicles only partially filled by calcite (Fig. 3a). The original mesostasis is partially replaced by authigenic intergrowths of calcite and K feldspar (Fig. 3a).

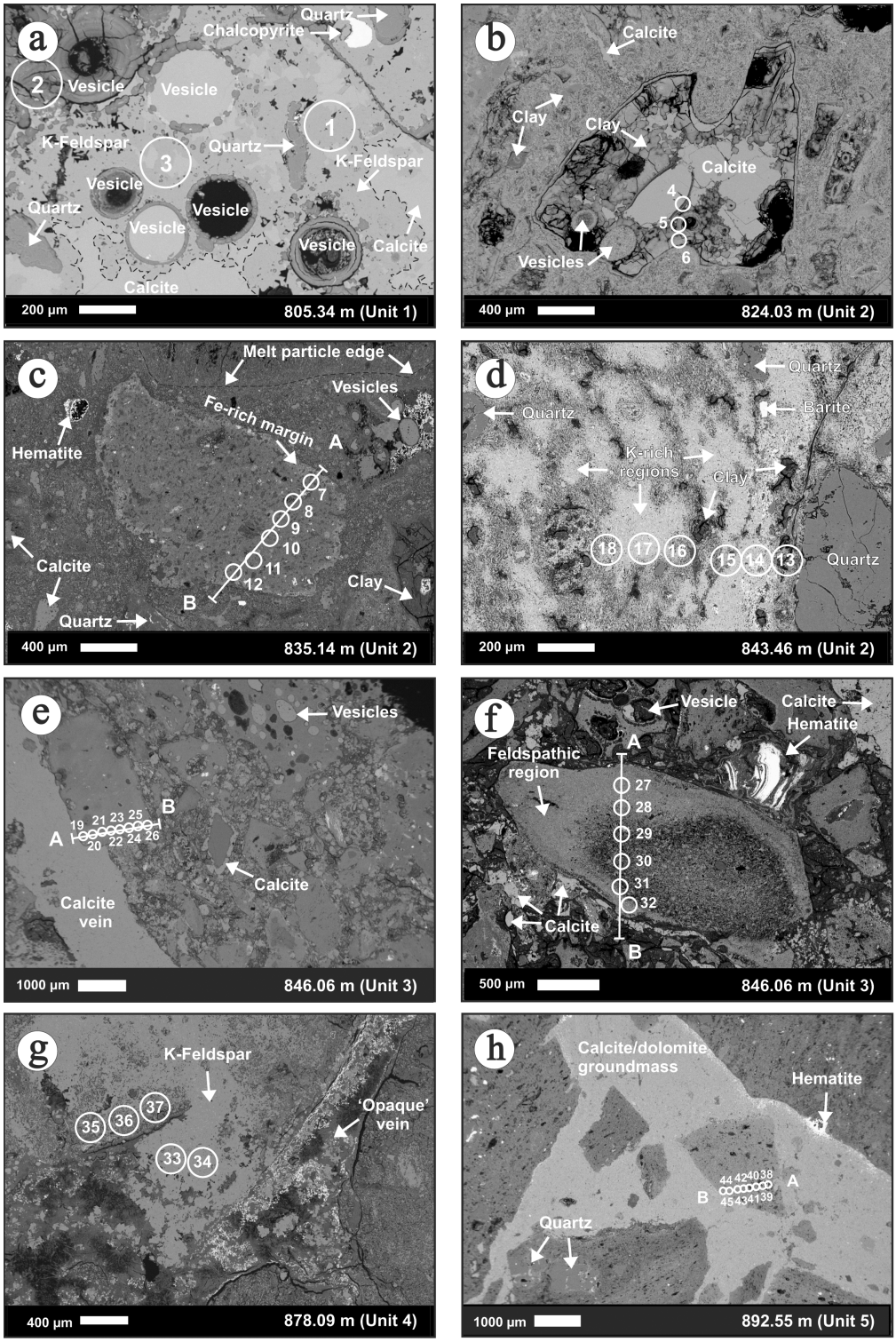

Fig. 3. Backscattered electron (BSE) images of melt particles analyzed in this study. The location of LA-ICP-MS ablation pits with analysis numbers are shown as large circles. a) Melt particle mrp_805.34, unit 1. Note the well-rounded cross-sections of vesicles, some infilled by calcite whereas others are empty. b) Melt particle mrp_824.03, unit 2. The interior region of the particle has been replaced by calcite. c) Melt particle mrp_835.14, unit 2. The margins of the particle are of higher BSE intensity, being rich in iron. d) Melt particle mrp_843.46, unit 2. The particle displays a patchy texture defined by bright BSE, K-feldspar-rich regions that are surrounded by phyllosilicate rich margins. e) Melt particle mrp1_846.06, unit 3. Note that a much lower proportion of groundmass is noted compared to the grains in Figs. 3c and 3d. f) Melt particle mrp2_846.06, unit 3. The particle shows marginal zonation defined by heavier elements compared to the core. g) Melt particle mrp_878.09, unit 4. h) Melt particle mrp_892.55, unit 5. Note the angular and shard-like character of the melt particles, which are groundmass-supported.

Unit 2

Three melt particles were analyzed from unit 2, from 824.03, 835.14, and 843.46 m depths (Figs. 3b–d, respectively). The shard-shaped particle in Fig. 3b is highly altered, shows a subangular morphology, and is partially replaced by calcite. Holes (irregularly shaped dark regions) are visible in the BSE image and are thought to have been plucked during thin sectioning. The melt particle at the center of Fig. 3c is well preserved and subrounded. The particle is zoned, having a narrow margin defined by a somewhat lighter gray color compared to the mottled interior. The BSE image of Fig. 3d is of a large, brown melt particle (>3 cm) and displays a patchy texture that is primarily controlled by sectors rich in K feldspar (see EMPA section 4.1).

Unit 3

Both melt particles analyzed from unit 3 are from a depth of 846.06 m (Figs. 3e and 3f). Figure 3e shows melt particles with subrounded to subangular shapes that contain vesicles. The particle analyzed (at left in the image) contains several BSE dark gray patches that are enclosed in a rather homogeneous, medium gray matrix. A bright (iron-rich) BSE region is noted at the bottom right of the particle. Figure 3f shows the second particle, which is subrounded and zoned as defined by medium gray BSE intensity towards the margin, compared to the darker gray core. Melt particles are well-compacted and contain vesicles (Fig. 3e), as well as calcite grains and veins. The groundmass is dark gray, suggesting it is composed of light elements (volatile-rich phyllosilicates).

Unit 4

Figure 3g represents the sample from 878.09 m depth in unit 4. A number of medium gray patches are discernible. High-magnification shows radiating acicular phyllosilicates, elongate and stubby microlites, and equant crystals of either adularia or orthoclase. Cross-cutting relationships between the microlites and larger equant crystals suggest the microlites crystallized first. The phyllosilicates do not cut the equant crystals, which suggests that the latter formed last. An opaque vein, typical of veining in the green monomict melt breccia, contains disseminated, μm-sized mrp-2 denote hematite and radiating acicular phyllosilicate crystals. The radiating crystal habit suggests rapid crystallization in open spaces.

Unit 5

Angular melt particles are typically suspended in the carbonate groundmass (Fig. 3h). The particles contain monomineralic quartz inclusions, dark alteration patches, BSE bright hematite patches, and numerous microlites. The latter may be preferentially aligned, indicative of flow prior to melt particle solidification and subsequent fragmentation. In the groundmass, hematite is observed at the margins of melt particles. Numerous small (<10 μm), angular melt particles occur disseminated in the groundmass carbonate minerals (see also Tuchscherer et al. 2004a).

GEOCHEMICAL RESULTS

Great care was taken to ensure that the LA-ICP-MS pits overlapped the much smaller EMPA spots in order to attempt correlation. The numbered circles shown in Fig. 3 represent ablation pits with corresponding LA-ICP-MS analysis numbers. The results are given in Tables 3 to 5 (Tables 3–5 are available online at http://meteoritics.org). In order to discuss the compositions of the melt particles, major elements have been plotted on an ACF-A'FK diagram (Fig. 4) and compositional profiles have been drawn (Fig. 5). With regards to the trace element data, chondrite-normalized REE patterns are compared (Fig. 6), and selected ternary diagrams (Fig. 7) and element ratio plots (Fig. 8) are used to illustrate compositional variation. The elements Zr, Sc, Nb, Y, Cr, Ni, and Co are all relatively immobile, and thus most useful for the investigation of possible protolith/proto-mineral chemical characteristics. The elements La, Sm, and Yb are incompatible, and thus provide a good comparison between severely altered and less-altered melt particles, as they preferentially migrate into a fluid phase. The large ion lithophile elements (LILE) Ba, Sr, and Rb are also incompatible, but because of their low ionic potential will behave during alteration differently from, for example, the rare earth elements (REE) (Guy et al. 1999). As observed in units 1 and 2 (Tuchscherer et al. 2004b), the LILE are preferentially enriched, as they have not been leached out due to their large ionic radii in comparison to the REE. The refractory elements Cr, Ni, and Co (Fig. 7c) also provide insight into the presence, or admixture, of mafic phases in the melt particles. For the identification of possible target components in the melt particle population, all currently known target rock compositions are compared in Figs. 7 and 8 with the melt particle data. For a similar correlation with the chondrite-normalized REE abundances and target rocks (Fig. 6), see the REE plots in Koeberl (1993) and Tuchscherer et al. (2004b, 2005).

Unit 1

The results of EMPA on the melt particle from 805.34 m depth have generally low wt% totals (analyses 1–19, Table 3), indicative of a high volatile content. The particle is characterized by low Ca and Na abundances but enriched in Fe, Mg, and K compared to compositions of melt particles from other units (with exception of the particle from 824.03 m). In Fig. 4, the data for this particle plot in a discrete group near the F apex of the ACF-A'FK diagram. Apart from this grouping, all major elements show some variation, especially regarding Ti, Al, and Fe. Trace element results for

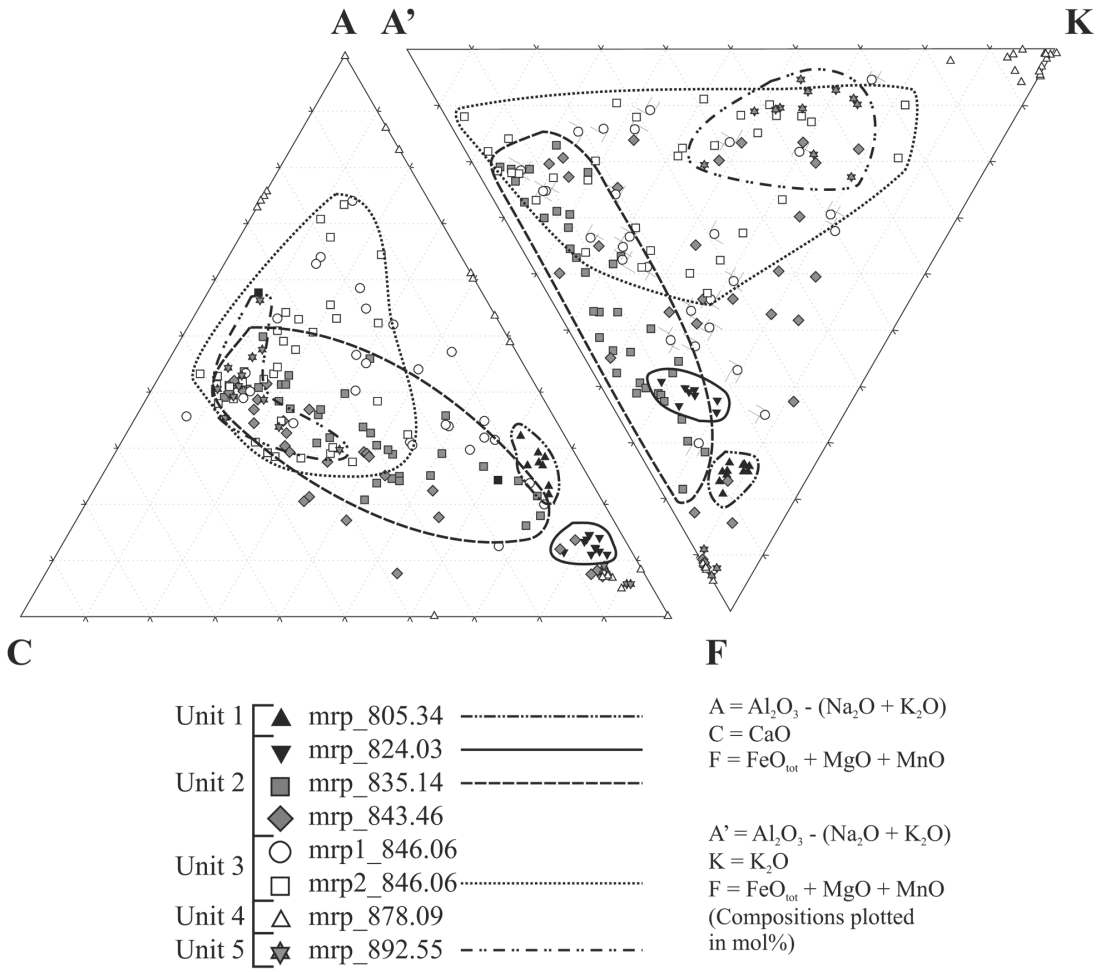

Fig. 4. ACF-A'FK diagram (after Eskola 1939) of Yax-1 melt particle compositions determined by EMPA (data from Table 3) and plotted based on molecular proportions.

the 805.34 m particle show some of the lowest trace element abundances obtained in this investigation, especially with regards to Ti, V, Co, Sr, Y, Nb, and the REE. The REE (Fig. 6a) abundance for this particle is almost chondritic; slight negative Ce and positive Eu anomalies are noted. Specific groupings can be discerned in the incompatible trace element data (Fig. 7a): the analyses form a high Zr and low Sc plus Y group. Lanthanum, Sm, and Yb (Fig. 7b), and Cr, Ni, and Co (Fig. 7c) do not yield groupings. Cr was not detected in most of these analyses, which therefore do not plot meaningfully in Fig. 7c. A plot of the LILE Rb, Sr, and Ba (Fig. 7d) also produces good compositional separation; the particle is low in Sr and high in Rb and Ba. Ratios of selected trace elements distinguish two data groups (Figs. 8a–8d). When comparing individual analyses with the sampled area (Fig. 3a), it is noted that there are no obvious compositional discrepancies between the altered melt particle and the orthoclase replacement intergrowths, with the exception of Ti that locally can be several orders of magnitude above average and signifies the presence of small inclusions.

Unit 2

The particle from 824.03 m depth has similar compositional characteristics as the particle from unit 1. Particle mrp_835.14 is rich in Si, Al, Ca, Na, and K (analyses 20–55, Table 3) and has an iron-rich margin, as observed in elevated BSE intensity (Fig. 3c) at the edges of the traverse (Fig. 5a). The surrounding groundmass is highly enriched in Ca, Mg, and Fe compared to the melt particle (analyses 1–11, Table 4, Fig. 5a). Abundances throughout the particle are highly variable (Fig. 5a). Only a single analysis produced an analytical total near 100 wt%, which is consistent with an andesine composition of $An_{49}Ab_{47}Or_4$ (analysis 48, Table 3). Most adjacent analyses are similar but contain some K and have low totals. In the ACF diagram (Fig. 4), most analyses fall between 30 and 50% C component, but some analyses scatter widely and trend towards the F apex; they originate from the Fe-rich margin of the particle. In the A'FK diagram, all analyses plot along the A'-F tie line, between 0 and 20% of the K component. Trace

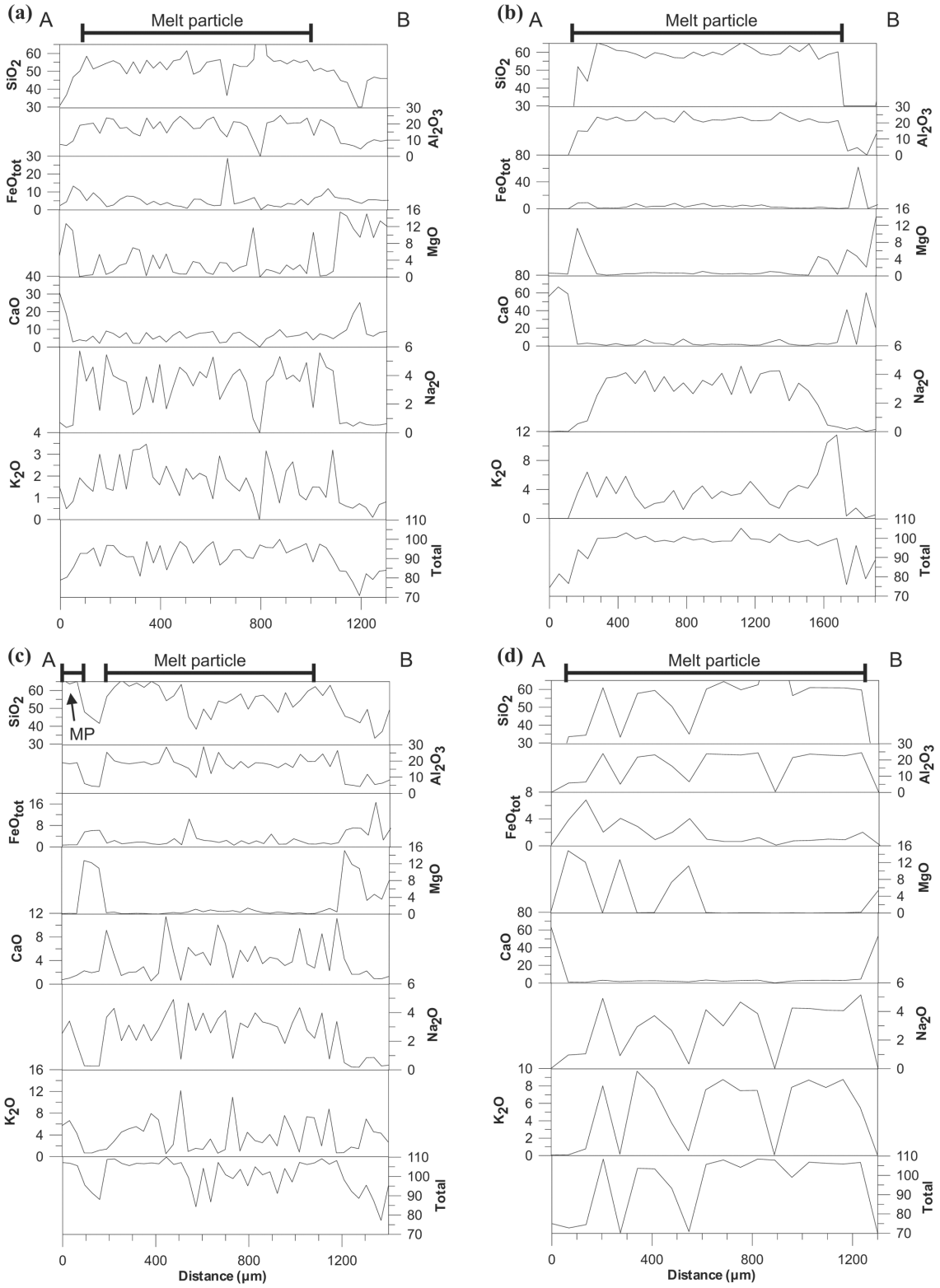

Fig. 5. a) Electron microprobe traverse through melt particle mrp_835.14: analyses 20–55 in Table 3 and analyses 1–11 of Table 4. b) Electron microprobe traverse through particle mrp1_846.06: analyses 86–114 of Table 3 and analyses 12–28 of Table 4. c) Electron microprobe traverse through particle mrp2_846.06: analyses 115–147 of Table 3 and analyses 29–38 of Table 4. Note that the zonation observed in Fig. 3f is best defined by SiO_2 and the wt% totals. d) Electron microprobe traverse through particle mrp_892.55: analyses 155–172 of Table 3 and analyses 39 and 40 of Table 4. Note that mafic phyllosilicates are most prevalent towards the "A" margin; the groundmass is calcite-rich.

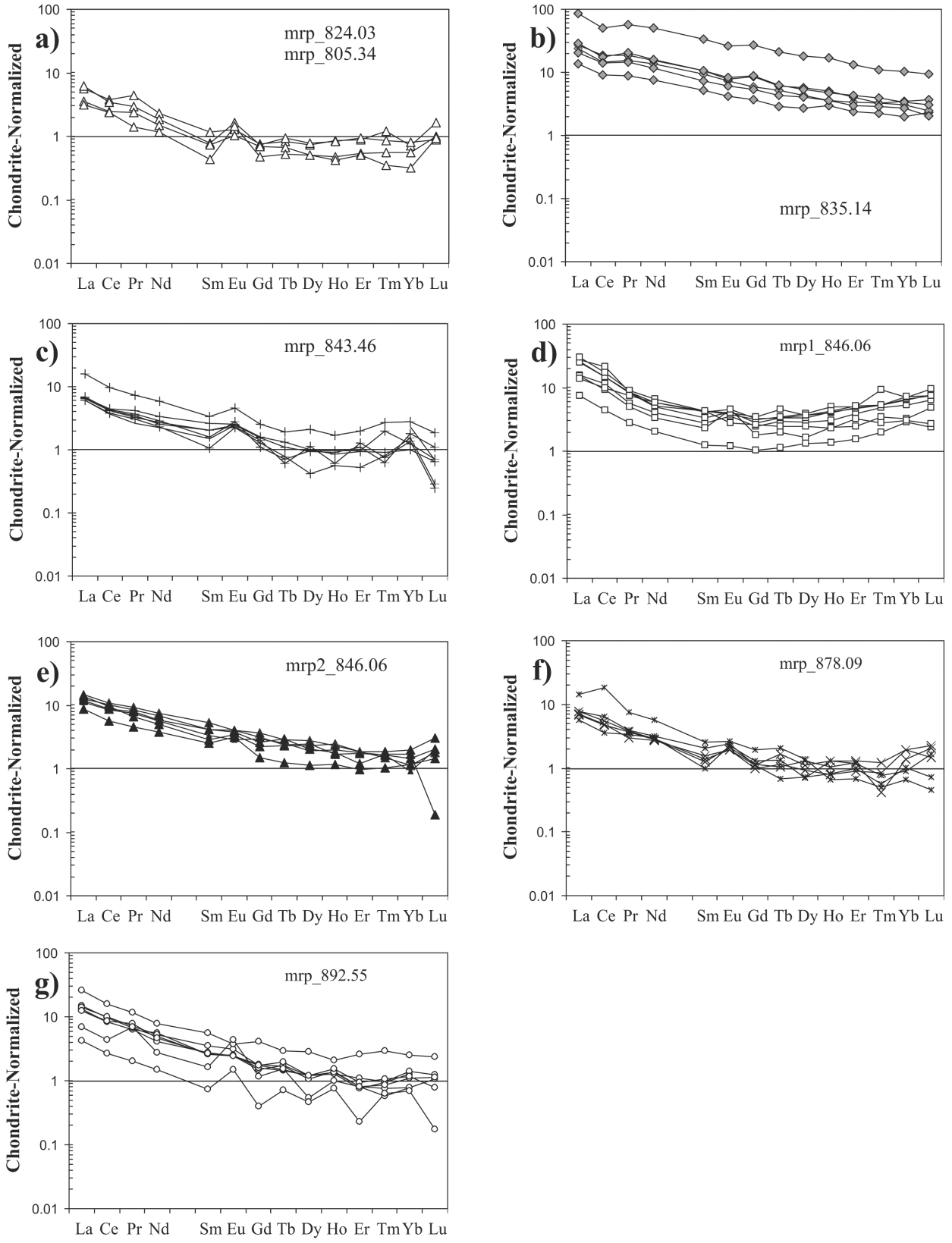

Fig. 6. Chondrite-normalized REE plots for the analyzed melt particles. a) Particles mrp_805.34 and mrp_824.03; b) mrp_835.14; c) mrp_843.46; d) mrp1_846.06; e) mrp2_846.06; f) mrp_878.09; g) mrp_892.55. Normalization values from Taylor and McLennan (1985).

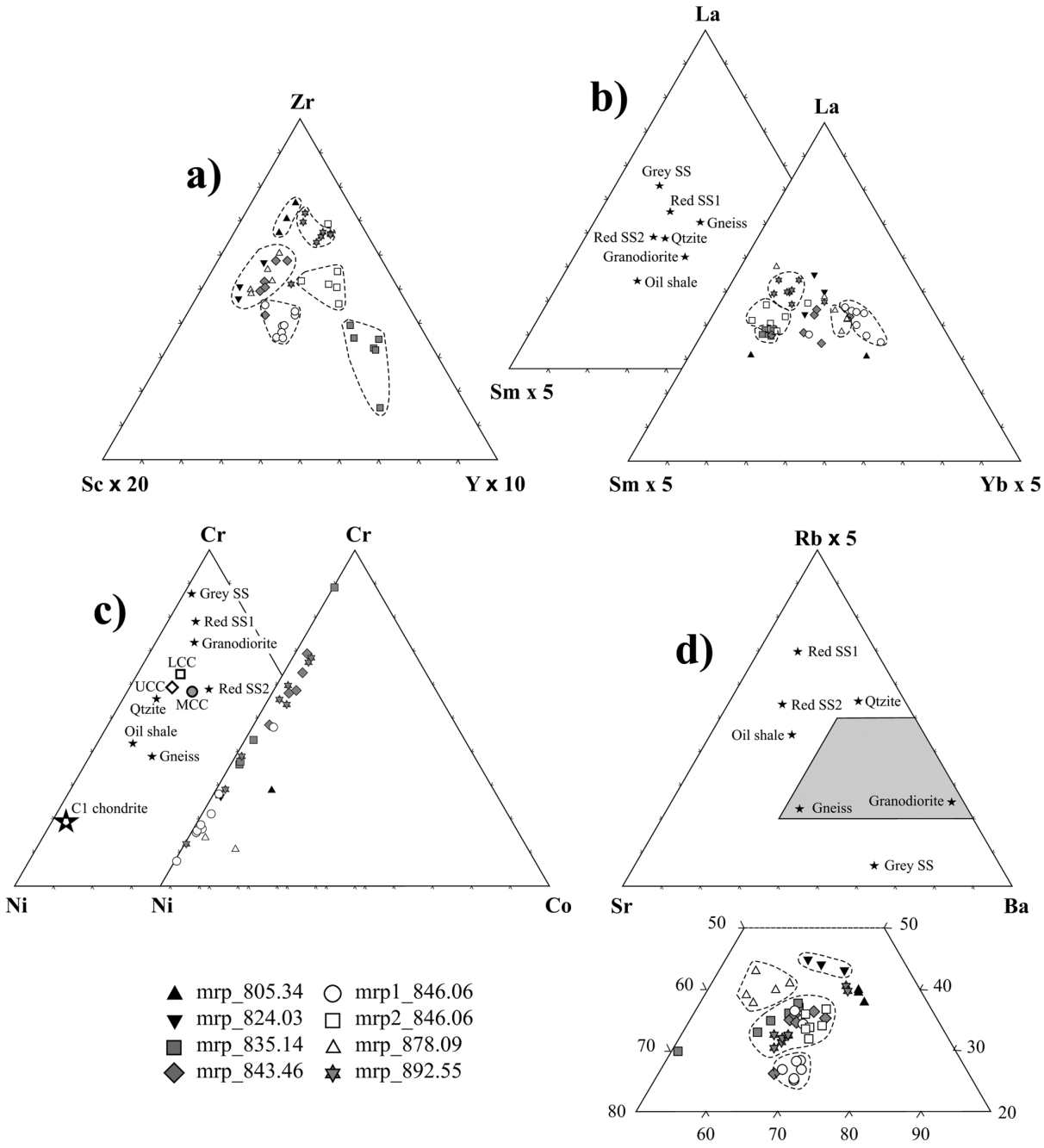

Fig. 7. Trace element ternary diagrams showing melt particle and known target rock compositions. Dashed areas indicate clusters of uniform melt particle compositions. a) Zr-Sc-Y ternary; in order to accentuate the melt particle fields, Sc and Y were factored by 20 and 10, respectively. b) La-Sm-Yb ternary; in order to accentuate the melt particle fields, Sm and Yb were both factored by 5. c) Cr-Ni-Co ternary, UCC = upper continental crust, MCC = middle continental crust, LCC = lower continental crust (crustal values from Rudnick and Gao 2003; CI chondrite values from Palme and Jones 2003). d) Rb-Sr-Ba ternary; in order to accentuate the melt particle field, Rb was factored by 5.

element results for particle mrp_835.14 (analyses 7–12, Table 5, unit 2) record some of the highest abundances in the whole data suite. The chondrite-normalized REE patterns show abundances up to 100× chondritic (Fig. 6b). Negative Ce but no Eu anomalies are noted. Specific groupings can be observed in the Zr-Sc-Y and La-Sm-Yb ternary diagrams (Fig. 7a and Fig. 7b), but more scatter is obvious in the Rb-Sr-Ba ternary (Fig. 7d). Particle mrp_835.14 is enriched in Y (Fig. 7a) and Sm (Fig. 7b) compared to all other analyzed particles. High Sm is indicated by the shallower slope of the LREE (Fig. 6b) and lower La/Sm ratios (Fig. 8d), also when compared to other melt particles. No grouping can be

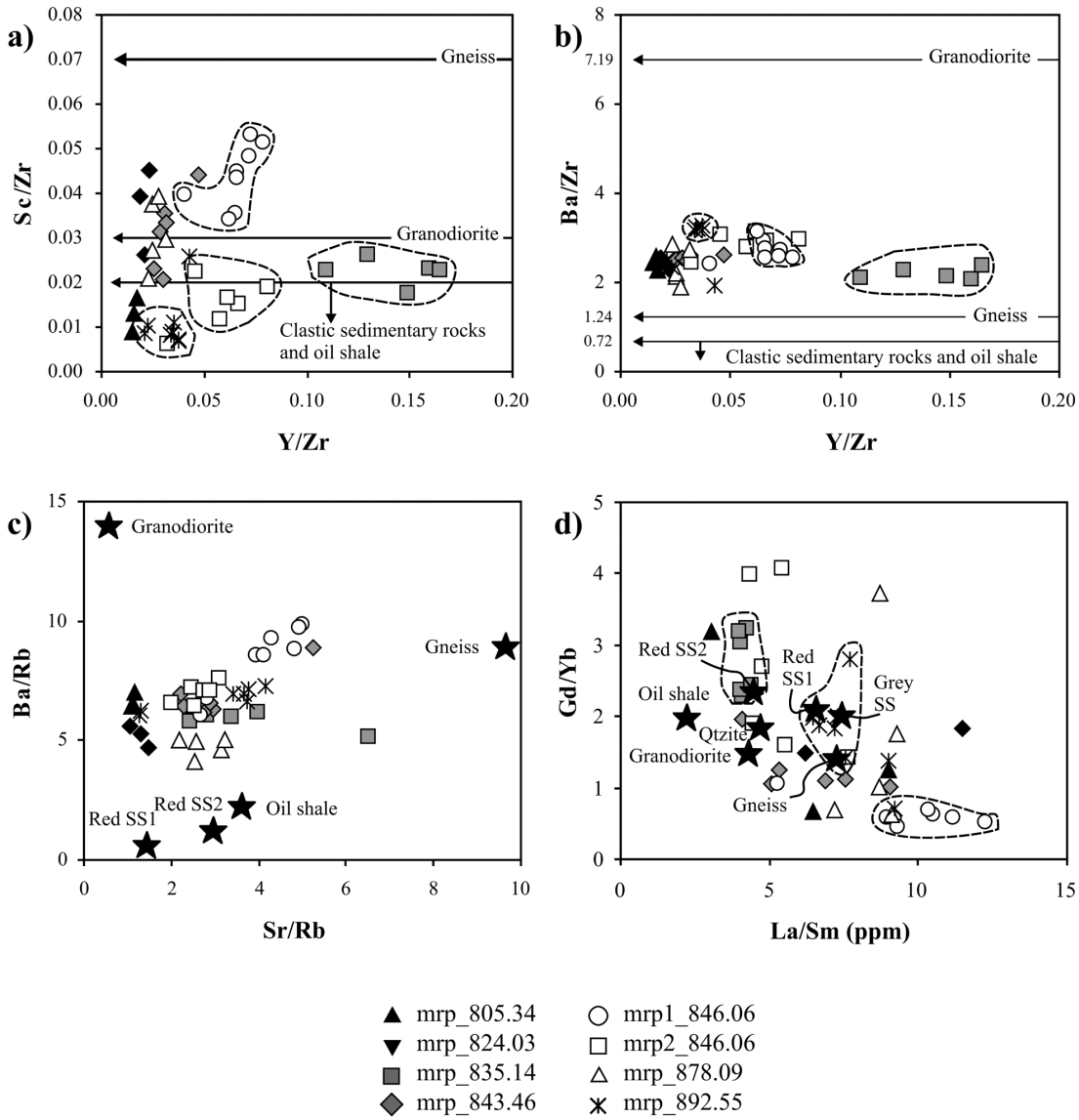

Fig. 8. Binary diagrams for melt particle and known target rock trace element ratios: a) Sc/Zr versus Y/Zr; b) Ba/Zr versus Y/Zr; c) Ba/Rb versus Sr/Rb; d) Gd/Yb versus La/Sm. See text for discussion.

identified in the distribution of Cr-Ni-Co (Fig. 7c), but reasonable groupings are observed in the element ratio plots (Figs. 8a, 8b, and 8d).

Microprobe analyses obtained from a brown melt particle (mrp_843.46, Fig. 3d) have in their majority (18/29) analytical totals near 100 wt%, indicating the particle is relatively volatile-poor (analyses 56–85, Table 3). These analyses correspond to a pseudo-feldspar composition of $An_{33}Ab_{32}Or_{35}$. Other EMP analyses rich in volatiles are consistent with a mixed mafic and alkaline composition. The analyses plot in the ACF diagram similar to particle mrp_835.14; however, because of the relatively high K abundances, these data scatter widely in the A'FK diagram (Fig. 4). The particle is not very trace-element-rich (analyses 13–18, Table 5, unit 2). Chondrite-normalized REE patterns are mostly above chondritic, but with some HREE analyses falling below or straddling the chondrite line (Fig. 6c). The LREE are preferentially enriched and a positive Eu anomaly is characteristic. Data for this particle are best separated from the analyses of other melt particles in the Zr-Sc-Y plot (Fig. 7a), but show much scatter in the La-Sm-Yb plot (Fig. 7b). A reasonable grouping occurs in the Rb-Sr-Ba plot; however, extensive overlap with data from other particles is noted. Trace element ratios produce relatively good groupings in Figs. 8a–c, but not in Fig. 8d.

Unit 3

The melt particle mrp1_846.06 (Fig. 3e, unit 3) has a generally feldspathic composition (analyses 86–114,

Table 3). Along the EMPA traverse the particle is relatively homogeneous with respect to silica (Fig. 5b) but has a lot of variation of Fe, Ti, Ca, Na, and K. Similar to the particle in Fig. 3c (mrp_835.14), this melt fragment is enriched in Si, Al, Na, and K compared to surrounding groundmass that is a carbonate/phyllosilicate mixture (analyses 12–28, Table 4). The melt particle analyses plot throughout the central areas of the ACF and A'FK diagrams, but not above 50% C component. This is attributed to low concentrations of Ca with increasing K (Fig. 4). Eight LA-ICP-MS analyses were obtained from this particle (analyses 19–26, Table 5). Overall abundances are relatively uniform, except for analysis 25 with a relatively lower concentration of the lithophile trace elements due to a local hematite patch of likely secondary origin. The chondrite-normalized REE diagram shows a concave (saddle) pattern, with all normalized abundances above chondritic values (Fig. 6d). In ternary plots the analyses fall into well-defined fields (Figs. 7a, 7b, and 7d). The siderophile elements (Fig. 7c) do not show any good compositional grouping. Other trace element ratios produce good groupings in Figs. 8a, 8c, and 8d, whereas three outliers are seen in Fig. 8b (variable Ba contents in analyses 19, 24, 26), two outliers in Fig. 8c due to low Sr abundances, and one outlier in Fig. 8d due to a low La/Sm ratio.

The zoned particle mrp2_846.06 is less volatile-rich in its marginal zone than in the core (Fig. 3f, unit 3). It is enriched in Si, Al, Ca, Na, and K (analyses 115–147, Table 3) compared to the groundmass, which is rich in Fe and Mg (29–38, Table 4). Figure 5c shows an EMPA traverse across the particle. In the central part, Si abundances are lower and more variable than at the margins, and Mg abundances are slightly higher in the core. The abundances of Fe, Ca, Na, and K are variable throughout the particle but relatively more so in the core. The particle is volatile-rich but, despite this, has a composition that resembles alkali feldspar. The melt particle does not contain much Fe or Mg; thus all analyses plot below 50% of the F components in both the ACF and A'FK diagrams; the data scatter (Fig. 4). Six trace element analyses were obtained for this particle (analyses 27–32, Table 5). REE patterns do not show much variation (Fig. 6e). The patterns are similar to those of mrp_835.14 but, in comparison, do not show a Ce anomaly and contain both positive and negative Eu anomalies. With regards to the observed zonation (Fig. 3f), analysis 30 in the central region of the melt particle shows slightly lower trace element abundances of P, Sc, Ti, V, Sr, and Y than the spots closer to the edge of the grain. Compositional groupings are observed in Figs. 7a, 7b, and 7d. No Cr was detected; thus, the particle can not be plotted in Fig. 7c. The LILE data yield a tight grouping, which overlaps with other melt particle compositional fields (Fig. 7d). Trace element ratio plots show good groupings in Figs. 8a–c, but scatter is prominent in Fig. 8d due to variable Gd/Yb ratios that are especially high at the edges of the particle. The lower trace element abundances in the central region of the particle correlate with lower EMPA totals.

Unit 4

A melt particle from 878.09 m depth represents the green impact melt breccia (Fig. 3g). Several EMP analyses were obtained in a relatively unaltered region, toward the top left of Fig. 3g, where plagioclase microlites of $An_{49–39}Ab_{57–44}Or_{7–3}$ composition occur. The particle also contains euhedral, equant orthoclase-like patches believed to represent secondary adularia from K-metasomatic overprint. In the A'FK diagram, these data all cluster towards the K apex (Fig. 4). In the ACF diagram, however, individual analyses plot along the A-C and A-F tie-lines, because Ca is either very low or absent, and Fe and Mg can also be absent. Several acicular diopside crystals of $En_{45–46}Fs_6Wo_{48–49}$ composition were found. This particle represents a specific melt type that is Ca- and Mg-rich enough to produce diopside microlites. The remainder of the particle, i.e., the altered mesostasis surrounding the orthoclase crystals, contains phyllosilicates rich in Mg (analyses 148–154, Table 3). The particle has relatively low trace element abundances (analyses 33–37, Table 5). The LREE are enriched, but do not exceed 10× chondritic values (Fig. 6f). The HREE scatter about the chondrite line, and all patterns have a positive Eu anomaly. Analysis 34 shows a strong positive Ce anomaly. Analyses of the immobile elements from the medium gray region (analyses 33 and 34) cluster together with the melt particle analyses (35–37) in the Zr-Sc-Y ternary diagram (Fig. 7a). The REE ternary plot shows more scatter for the orthoclase patch than the melt particle analyses, the latter plotting together (Fig. 7b). No grouping occurs for Cr, Ni, and Co results (Fig. 7c), but the LILE analyses all plot together (Fig. 7d). Trace element ratio plots show much scatter in Figs. 8a, 8b, and 8d, and a relatively good grouping in Fig. 8c.

Unit 5

Particle mrp_892.55 is alkali-rich and characterized by a variable volatile content, (total major element contents range from 60 to 97 wt%; analyses 155–169, Table 3). This is primarily the result of mafic phyllosilicates interspersed with alkali-rich melt. The Al, Na, and K abundances are anti-correlated with Fe and Mg contents. A traverse shows that the mafic patches are located mostly at the A margin (Fig. 5d). This produces two data groupings in the ACF diagram, one near the F apex and another closer to the A-C tie line (Fig. 4). In the A'FK diagram, the alkali-rich phases plot close to the K apex. Trace element results are variable (analyses 38–45, Table 5). REE concentrations vary widely from below chondritic values to 20 times above. Six patterns have positive Eu anomalies (Fig. 6g). Compositional groupings occur in Figs. 7a, 7b, and 7d. Variable ratios of Cr and Ni are noted (Fig. 7c). Analysis 40 has high P, Sc, Ti, V, Cr, Ni, Co, Y, Zr, Nb, REE, low Ba, and a high Sc/Zr ratio. These high abundances most likely reflect the local presence of titanite. This analysis also forms a compositional outlier in Figs. 7a

and 8a. Two analyses, 38 and 39, have relatively low trace element abundances, especially for Sr, and thus plot away from the other analyses (Figs. 7d, 8b, and 8c). These aberrant data were obtained close to the right margin labeled "A" (Fig. 3h), which is rich in mafic phyllosilicate phases, as determined by optical examination and EMPA (Fig. 5d).

DISCUSSION

EMPA and LA-ICP-MS analysis has provided new insight into the composition of melt particles of the Yax-1 drill core, especially with regard to the trace element distribution at the microscopic scale. Several previous investigators noticed the heterogeneous and pervasive alteration signature in the Yax-1 impactites (see geochemistry background in the Introduction section). However, because the melt particles were subjected to variable degrees of alteration, other techniques have to be used to unmask the melt formation process(es). Here, we discuss how LA-ICP-MS trace element data can help decipher the genetic history of these highly altered melt phases.

EMPA Constraints on Secondary Alteration

Besides the limited number of EMP analyses from this and earlier studies that yielded analytical totals near 100 wt%, the database suggests that all remaining melt particle analyses with low analytical totals represent compositions that have been overprinted by secondary hydrothermal processes and/or were devitrified through diagenetic hydration (e.g., Ames et al. 2004; Hecht et al. 2004; Tuchscherer et al. 2004a, 2004b, 2005; Zurcher et al. 2004). The Chicxulub impactor struck a wet and carbonate-rich target that inevitably promoted the formation of volatile-rich melt particles and their alteration after cratering. Melt particles from units 1 and 2 are depleted in Ca and Na but enriched in Fe, Mg, and K in comparison with melt particles from greater depth. Because of their stratigraphic location at the top of the impactite section and the similar geochemical alteration signature as that of palagonized volcanic rocks (e.g., Guy et al. 1999), we believe that the upper impactites interacted with seawater. This has promoted compositional homogeneity of the melt particles in the upper two units, which are of more uniform composition compared to particles from the lower units (see compositional fields and sample depths in Fig. 4). This homogenization effect can also be observed in the whole rock major and trace element data for this unit (Tuchscherer et al. 2004b).

Electron microprobe analyses with low analytical totals, indicative of strong alteration, have also been obtained from melt particles and groundmass phases from below unit 2 (e.g., analyses with low wt% totals and rich in Mg and Fe from particles mrp_843.46, mrp_878.09, and mrp_892.55) (Tables 3 and 4). These analyses also typify the preferential leaching of Na and K observed throughout the impactite sequence, but not as thoroughly as in units 1 and 2. The zonation in melt particle mrp_846.06 is representative of this process, which most likely is the result of diffusion of Na and K from the adjacent volatile-rich groundmass (Fig. 3f).

Other secondary phases encountered here are adularia and calcite, which are commonly found in melt particles throughout the impactite sequence (also Hecht et al. 2004; Zurcher et al. 2004). Anomalous Fe abundances along melt particles margins have been observed in melt particle mrp_835.14 and mrp_892.55 and testify to the mobility of this element. This was shown by Pilkington et al. (2004), who recognized the dominant magnetization in Yax-1 impactites originated from secondary magnetite. The occurrence of secondary alteration phases and the redistribution of Fe, Na, K, and volatiles all contribute to the heterogeneity of melt particle compositions at the microscale, as successfully investigated by EMPA. However, thus far, this technique alone has not been able to succeed in deciphering any primary formation processes for these melt particles.

Linking EMPA and LA-ICP-MS Results

Our EMPA and LA-ICP-MS results indicate that melt particles are of highly diverse compositions, which renders melt particle compositional classification difficult. Some LA-ICP-MS analyses yield abundances orders of magnitude greater than adjacent analyses (e.g., analyses 11, 14, 27, and 40 of particles mrp_835.14, mrp_843.46, mrp_846.06, and mrp_892.55), which we attribute, at least partially, to a "nugget" effect from trace-element-rich accessory phases such as zircon, apatite or titanite, the presence of which was ascertained by individual EMP analyses. Cathodoluminescence observations also show the presence of apatite schlieren that are poorly mixed with the enclosing melt and/or isolated apatite and zircon grains within melt particles (Tuchscherer et al. 2004a). Conversely, analyses with relatively lower trace element abundances may be attributed to microscopic phases that are inherently poor in trace elements, i.e., calcite, hematite, or areas rich in phyllosilicates (e.g., analyses from units 1 and 2, and analyses 25, 30, 38, and 39).

Only two trace elements, titanium and chromium, were analyzed with both techniques. Their abundances in the two data sets do not, however, correlate with the LA-ICP-MS results typically having much lower values than the corresponding EMPA data. This is likely a result of the different volumes of material analyzed. For example, melt particle mrp_835.14 contains two areas with high Ti (see Table 3). The only LA-ICP-MS analysis that shows any high Ti is analysis 11 (Table 5), which does not overlap with the EMPA Ti-rich area near the A point of the traverse. The EMPA compositional heterogeneities can only serve to explain suspected heterogeneities observed in the LA-ICP-MS data. Any direct correlation is coincidental; i.e., high LA-ICP-MS trace element results do not necessarily correspond to high EMPA Ti and Cr results.

Trace Element Constraints on Secondary Alteration

In order to further investigate the nature and degree of alteration of the melt particles, variations between the immobile elements Sc, Zr, Y, the more mobile incompatible REE, and the very mobile LILE are considered. Melt particles that show good compositional groupings of the immobile, REE, and mobile trace elements (LILE) may be interpreted as relatively unaltered and are also homogeneous in composition, on the LA-ICP-MS scale (compare Figs. 7 and 8). This includes particles mrp_835.14, mrp1_846.06, and mrp_878.09, and this signature is referred as type 1 composition. If a particle shows groupings of immobile elements but not in the REE or LILE plots, this suggests that the particle is altered to a degree; this refers to particles mrp_805.34 and mrp2_846.06 and is referred as type 2 composition. Particles that show much variation in the immobile, REE, and LIL elements can be interpreted to have primary compositional heterogeneity and are called type 3. Particle mrp_843.46 belongs to this category. A melt particle that shows variations in the immobile elements but reasonable groupings with regard to either the REE or LILE was likely subject to secondary overprint, like particles mrp_824.03 and mrp_878.09; this is termed type 4. The difference between types 2 and 4 is that the former has been leached by seawater, whereas the latter has been metasomatized by a K-, LILE-, and/or REE-rich fluid. This systematic approach can not, however, determine whether melt particles of type 3 composition are either of primary or secondary compositional diversity.

For melt particle mrp_835.14 with the highest recorded overall trace element abundances, the EMPA results are highly variable and mostly indicate a high volatile content. There does not appear to be a relationship between high trace element abundances and the alteration state of melt particles. Negative Ce anomalies in REE analyses of unit 1 and 2 melt particles indicate leaching by seawater through preferential removal of Ce^{3+} (Guy et al. 1999; Utzmann et al. 2002). This anomaly is observed in all analyzed particles to a sample depth of 835.14 m. Cerium has a partitioning coefficient four times greater than that of La (Guy et al. 1999; Utzmann et al. 2002), and will thus be mobilized into an aqueous phase more readily than the other REE. However, this does not appear to correlate with results from bulk rock REE analyses (Tuchscherer et al. 2004b), which suggest some of the remobilized Ce must be contained in either the groundmass or secondary phases in these units. This is consistent with small-scale mobilization of Ce. The carbonate component of the impactites, inferred by the carbonate end-member composition of Tuchscherer et al. (2005), shows a strong negative Ce anomaly. It implies that the leached Ce should be accommodated by a silicate phase similar to zeolites and saponite in altered basalt (Guy et al. 1999). Analyses enriched in Ce are also found in lower impactites (particles mrp1_846.06 and mrp_878.09), perhaps indicative of precipitation of insoluble Ce^{4+} in a recharge zone characterized by Ce^{3+} oxidation.

Protoliths/Proto-Minerals and Mixing of Precursor Phases

Because of the highly heterogeneous composition of the melt particles, it is apparent that they do not explicitly represent bulk rock melts, but possibly mixtures of anything between individual mineral melts and mixed rock melts. This interpretation is supported by the fact that stoichiometric plagioclase of andesine ($An_{49}Ab_{47}Or_4$) composition has been measured in particle mrp_835.14 and a K feldspar-plagioclase mixed composition of $An_{33}An_{32}Or_{35}$ was found in particle mrp1_846.06. We do not believe these melt particles were subjected to extensive alkali metasomatism, as they are both of type 1 composition based on our trace element alteration discrimination technique. A mixed orthoclase with iron melt composition is suggested by melt particle mrp_843.46, but it can not be excluded that this is due to secondary overprint. For the remaining analyses, which mostly have low major element totals, it is difficult to discern their original composition and then extend the interpretation to possible precursor phase(s). Heterogeneous melt particle compositions have been interpreted to be characteristic of suevites formed by impacts in lithologically varied target rocks (Dressler and Reimold 2001). If the Yax-1 melt particles are interpreted as melts of individual minerals or of mixtures of minerals, compositions can even exceed the complexity of the target, due to incomplete mixing of individual melts. Of course, secondary alteration processes are a further complication.

Another method that can be used to constrain possible precursor materials involves the use of trace element ratios (Figs. 7 and 8). Compositions of known target rocks (granodiorite, gneiss, clastic sedimentary rocks, and oil shale) can be used for comparison with the compositions of the melt particles (Table 6). It is observed that the Sc/Zr ratios of the melt particles (Fig. 8a) are constrained between the ratio of gneiss from the Yax-1 borehole and various clastic sedimentary rock compositions (Koeberl 1993). This must also include a mafic component (likely amphibolite) (Kettrup et al. 2003). The highest known target rock value of Ba is 7.19 for a granodiorite clast (Fig. 8b). Therefore, the low Ba/Zr ratios of melt particles could indicate a predominant metasedimentary or gneissic protolith with Ba/Zr ratios <1.24. However, the preferential remobilization and leaching of Ba cannot be excluded.

LILE ratios Ba/Rb and Sr/Rb show relatively good compositional groupings for the individual melt particles, and these values are also constrained by currently known target rock compositions, i.e., all melt particle compositions are intermediate between known target rock compositions (Figs. 7d and 8c). REE data show significant scatter and thus appear to have been affected by secondary alteration (Figs. 6, 7b, and 8d). Also, no currently known target rock composition

Table 6. Selected trace element concentrations for known target rocks related to the Chicxulub impact crater (in ppm).

	Granodiorite[a]	Gneiss[a]	Avg. oil shale[a]	2 sigma	Red SS1[b]	Red SS2[b]	Gray SS[b]	Qtzite[b]
Sc	4.4	12.5	5.7	3.7	4.74	4.61	0.66	2.13
Cr	32.9	19.5	65	46.4	27.8	28.1	23.3	23.4
Co	4.48	8.08	14	10	2.52	9.89	0.53	3.62
Ni	8	23	74	20	5	10	3	15
Rb	66.5	30.5	31.2	26.3	68.3	42.9	3.72	13.2
Sr	36	287	117	37	100	125	95	<30
Zr	135	185	232	103	460	450	250	670
Ba	970	229	74	72	50	55	180	40
La	7.2	29.2	4.5	2.8	22.4	22.3	15.7	31.6
Sm	1.66	3.98	1.85	0.8	3.43	4.98	2.01	6.67
Gd	1.75	4.8	1.4	0.52	3.7	4.6	1.3	6.4
Yb	1.21	3.61	0.67	0.2	1.71	1.96	0.65	3.31
Ratios								
Sc/Zr	0.03	0.07	0.02	–	0.01	0.01	0.003	0.003
Ba/Zr	7.19	1.24	0.32	–	0.11	0.12	0.72	0.06
Ba/Rb	14.59	7.51	2.37	–	0.73	1.28	48.39	3.03
Sr/Rb	0.54	9.41	3.75	–	1.46	2.91	25.54	n/a
La/Sm	4.34	7.34	2.43	–	6.53	4.48	7.81	4.74
Gd/Yb	1.45	1.33	2.09	–	2.16	2.35	2	1.93

[a]Tuchscherer et al. (2005).
[b]Koeberl (1993).
Avg = average, SS = sandstone, Qtzite = quartzite.

can account for the high La/Sm and Gd/Yb ratios observed in the melt particles (Fig. 8d). Combinations of known target rocks also cannot account for the observed melt particle REE characteristics, as combinations by averaging or direct addition of ratios cannot exceed any current target rock compositions. Ratios of trace elements can only be modified by primary differentiation processes or the preferential hydrothermal remobilization of certain elements.

Our analyses are generally Co-poor, compared to Ni and Cr that show an apparent mixing trend (Fig. 7c), which can not, however, be attributed to any currently known Ni-bearing target rocks. This likely confirms that the mafic component of the target stratigraphy has not been sampled properly. A small proportion of projectile matter could also contribute to this trend; the projectile contribution to the suevitic impact breccias was estimated by Gelinas et al. (2004) at ~0.1%. This would result in a contribution of some 0.5 ppm Co, 10.8 ppm Ni, and 2.6 ppm Cr from a CI meteorite (Palme and Jones 2003), the type inferred for the K/T bolide by Shukolyukov and Lugmair (1998) from Cr isotopic analysis. The highest siderophile element abundances in the Yax-1 borehole have been determined in narrow shale horizons (Tuchscherer et al. 2005), which make up an insignificant proportion of the Yucatán pre-impact target rocks (Ward et al. 1995). These samples do not possess an adequate Ni/Cr ratio to account for the observed trend. However, known values for the upper, middle, and lower continental crust (Rudnick and Gao 2003), as well as for average CI chondrite, plotted in Fig. 7c may explain the observed trend by a mixture of continental crust and the projectile.

Melt Particle Formation

Petrographic observations of melt particles yield clues to their formation. It is suggested that small particles (<0.5 mm) cooled rapidly and, thus, were deposited as quenched shard-like fragments that were then enclosed by the groundmass. Vesicular nature, angular morphologies, and small sizes testify to formation in a volatile-rich and extremely turbulent environment prior to deposition and/or consolidation with the groundmass. Rapid quenching is also necessary to maintain the heterogeneous compositions of individual melt particles. Melt particles larger than 0.5 mm could have kept enough latent heat to allow them to be deposited while in a semiplastic state, i.e., above the glass transition temperature. This semimolten state would have allowed melt particles below unit 2 to flow and solidify with schlieren textures. However, it is possible that schlieren could also have formed through the agglomeration of various melts while in transit through the air. The protracted cooling period also allowed the crystallization of microlites, which increase in proportion with core depth (Tuchscherer et al. 2004a)—likely because melt particles lower in the impactite sequence took longer to cool. The melt particles from unit 5, however, all show angular morphologies but lack vesicles, which indicates rapid cooling and extensive fragmentation prior to deposition in a relatively dry or higher pressure environment. Most particles in unit 5 also show well-preserved microlites. This indicates that once the shard-like particles were deposited, microlite growth persisted under slower cooling conditions. This may have been induced by thermal conduction from the overlying

impact melt rock of unit 4. Engelhardt et al. (1995) showed experimentally that quenched melt particles in the Ries crater could continue to crystallize plagioclase microlites below the glass-transformation temperature to a temperature of 550 °C at 600 bar water pressure. Similar conditions may have been present here to allow microlites to crystallize in the angular melt particles of unit 5.

Melt particles from unit 1, on the other hand, are all subrounded, with only rare particles revealing well-preserved vesicles and shard-like morphologies. As indicated by Goto et al. (2004) and discussed by Tuchscherer et al. (2004a, 2004b, 2005), these particles were most likely redeposited and reworked by seawater resurge into the crater basin, minutes after impact and suevite deposition. This idea is in contrast to Stöffler et al. (2004), who did not consider aquatic reworking. The melt particles must have quenched rapidly, as no microlites are observed in this unit.

Volatiles in the target rocks at Chicxulub appear to have been essential for preserving the heterogeneous compositions of melt particles. Volatiles (H_2O, CO_2, SO_x) would have enabled the dispersion of the particles, thus inhibiting homogenization (Kieffer and Simonds 1980; Hörz et al. 2002). The Yax-1 suevites have a large carbonate component, but no significant SO_3 concentrations have been found despite the significant anhydrite component of the target. This suggests all sulfates were devolatized upon impact (Tuchscherer et al. 2004b). The evidence for the melt particles having interacted with volatiles can be found in their extensively altered nature, such as, for example, the conversion to phyllosilicate phases, and the occurrence of abundant filled vesicles in the upper three units. The dispersion of fallback suevite also facilitated the rapid cooling of melt particles, producing heterogeneous melt particle compositions.

Comparison with Melt Rocks from Other Impact Structures

Impacts into lithologically diverse targets can produce compositionally heterogeneous melt particles in suevite, especially at the microscale (see Dressler and Reimold 2001). Large impacts can access quite heterogeneous crust. For example, Dressler et al. (1996) showed that melt particles obtained from the Onaping Formation, widely considered the suevite deposit of the Sudbury Structure, have compositions that are highly heterogeneous and represent diaplectic and liquid-state glasses that quenched rapidly after shock melting of the lithologically varied target sequence. A recent study of Ries melt particles and glasses by Osinski (2003) showed that various types of glasses exist in the Ries suevite, which also originated from the melting of different target lithologies. A detailed EMPA investigation of ballistically dispersed melt particles from Meteor Crater resulted in the recognition of heterogeneous melt particle compositions (Hörz et al. 2002). These authors suggested that efficient mixing was hindered by the devolatilization of CO_2 from the shock melting of target carbonate rocks—an important target component in the case of the Ries and the Chicxulub structures as well. Our results are thus consistent with suevite deposits that are found in large impact structures that have heterogeneous target rocks.

SUMMARY AND CONCLUSIONS

Constraints from this study provide insight into the formation of melt particles, mixing characteristics between various melts and lithic inclusions, and alteration characteristics. The main results are:

1. Stoichiometric feldspar and plagioclase compositions found in melt particles indicate mineral melting during cratering, whereas mixed alkali feldspar and plagioclase compositions show mixing of mineral melts.
2. The compositional heterogeneity of melt particles can exceed the compositional diversity of the target rocks because of incomplete mixing between mineral melts and/or rock melts.
3. Melt particles that have been leached by seawater (units 1 and 2) are of a more homogeneous composition than particles located lower in the impactite sequence; they show negative Ce anomalies.
4. Heterogeneous trace element compositions are the product of alteration, the incomplete melting of precursor phases (nugget effect), incomplete mixing of melts (schlierens), and the presence of small clasts.
5. Correlation of the EMPA and LA-ICP-MS data is problematic due to the disparate beam widths of the two techniques.
6. Trace element results allow the compositional discrimination of melt particles based on groupings for immobile elements, REE, and LILE data. Four type compositions have been assigned on trace element basis that help determine the variable degrees of alteration.
7. Trace element ratio plots for data obtained from melt rock particles overlap with all known target rock compositions and, thus, support that these melt particles represent various target rock mixtures. No such overlap can be observed with ratios of the REE (Gd/Yb and La/Sm), either because of secondary remobilization or an incomplete target rock trace element geochemical record.
8. Siderophile element, especially Ni and Cr, data indicate mixing involving Cr,Ni-rich components. No trace element data currently exist for the postulated mafic target rocks. A small contribution could originate from the bolide.
9. Small shard-like melt particles in units 1 to 3 quenched rapidly in a volatile-rich environment prior to solidification with the host groundmass. Larger fluidal melt particles that contain microlites underwent protracted cooling. Shard-like melt particles in unit 5 contain microlites and are believed to have crystallized

below the glass transformation temperature or were fragmented after crystallization.

10. The presence of volatiles in target rocks helped disperse and cool melt particles during cratering. Impacts that occur in target rocks of variable composition and that are rich in volatiles (Chicxulub, Sudbury, Ries, Meteor Crater) are more likely to develop suevite deposits with heterogeneous melt particle compositions.

Acknowledgments–We gratefully acknowledge the comprehensive financial support by the American Chemical Society Petroleum Research Fund (grant PRF # 37299-AC8), and the support of the Director of the Council for Geoscience (CGS), Pretoria. Maria Anastova and Annabe Walliser (CGS) provided helpful guidance during SEM and EMP analysis, respectively. We are also very grateful for the insightful and constructive editorial reviews of Pierre Beck, Paul Sylvester, and John Spray that significantly improved this article. M. G. T. thanks, in particular, his wife Libby Sharman-Harris for her continuous support. This is Impact Cratering Research Group Contribution No. 98.

Editorial Handling—Dr. John Spray

REFERENCES

Ames D. E., Kjarsgaard I., Pope K. O., Dressler B., and Pilkington M. 2004. Secondary alteration of the impactite and mineralization in the basal Tertiary sequence, Yaxcopoil-1, Chicxulub impact crater, Mexico. *Meteoritics & Planetary Science* 39:1145–1167.

Dressler B. O., Weisser T., and Brockmeyer P. 1996. Recrystallized impact glasses of the Onaping Formation and the Sudbury Igneous Complex, Sudbury Structure, Ontario, Canada. *Geochimica et Cosmochimica Acta* 60:2019–2036.

Dressler B. O. and Reimold W. U. 2001. Terrestrial impact melt rocks and glasses. *Earth-Science Reviews* 56:205–284.

Dressler B. O., Sharpton V. L., Morgan J., Buffler R., Moran D., Smit J., Stöffler D., and Urrutia-Fucugauchi J. 2003. Investigating a 65-Ma-old smoking gun: Deep drilling of the Chicxulub impact structure. *Eos* 84:125–131.

Dressler B.O., Sharpton V. L., Schwandt C. S., and Ames D. 2004. Impactites of the Yaxcopoil-1 drilling site, Chicxulub impact structure: Petrography, geochemistry, and depositional environment. *Meteoritics & Planetary Science* 39:857–878.

Engelhardt W. V., Arndt J., Fecker B., and Pankau H. G. 1995. Suevite breccia from the Ries crater, Germany: Origin, cooling history and devitrification of impact glasses. *Meteoritics* 30:279–293.

Eskola P. 1939. *Die Entstehung der Gesteine.* Berlin: Julius Springer. 422 p.

Gelinas A., Kring D. A., Zürcher L., Urrutia-Fucugauchi J., Morton O., and Walker R. J. 2004. Osmium isotope constraints on the proportion of bolide component in Chicxulub impact melt rocks. *Meteoritics & Planetary Science* 39:1003–1008.

Goto K., Tada R., Tajika E., Bralower T. J., Hasegawa T., and Matsui T. 2004. Evidence for ocean water invasion into the Chicxulub crater at the Cretaceous/Tertiary boundary. *Meteoritics & Planetary Science* 39:1233–1247.

Grégoire M., Bell D. R., and Le Roex A. P. 2002. Trace element geochemistry of phlogopite-rich mafic mantle xenoliths: Their classification and their relationship to phlogopite-bearing peridotites and kimberlites revisited. *Contributions to Mineralogy and Petrology* 142:603–625.

Guy C., Daux V., and Schoot J. 1999. Behaviour of rare earth elements during seawater/basalt interactions in the Mururoa Massif. *Chemical Geology* 158:21–35.

Hecht L., Wittman A., Schmitt R. T., and Stöffler D. 2004. Composition of impact melt particles and the effects of post-impact alteration in suevitic rocks at the Yaxcopoil-1 drill core, Chicxulub crater, Mexico. *Meteoritics & Planetary Science* 39: 1169–1186.

Hörz F., Mittlefehldt D. W., See T. H., and Galindo C. 2002. Petrographic studies of the impact melts from Meteor Crater, Arizona, USA. *Meteoritics & Planetary Science* 37:501–531.

Kamo S. L. and Krogh T. E. 1995. Chicxulub crater source for shocked zircon crystals from the Cretaceous-Tertiary boundary layer, Saskatchewan: Evidence from new U-Pb data. *Geology* 23: 281–284.

Kettrup B. and Deutsch A. 2003. Geochemical variability of the Yucatán basement: Constraints from crystalline clasts in Chicxulub impactites. *Meteoritics & Planetary Science* 38: 1079–1092.

Kieffer S. W. and Simonds C. H. 1980. The role of volatiles and lithology in the impact cratering process. *Reviews in Geophysics and Space Physics* 18:143–181.

Koeberl C. 1993. Chicxulub crater, Yucatán: Tektites, impact glasses, and the geochemistry of target rocks and breccias. *Geology* 21: 211–214.

Kring D. A., Hörz F., Zurcher L., and Urrutia Fucugauchi J. 2004. Impact lithologies and their emplacement in the Chicxulub impact crater: Initial results from the Chicxulub Scientific Drilling Project, Yaxcopoil-1, Mexico. *Meteoritics & Planetary Science* 39:879–897.

Le Roux P. J., Le Roex A. P., and Schilling J.-G. 2002. MORB melting processes beneath the southern Mid-Atlantic Ridge (40–55°S): A role for mantle plume-derived pyroxenite. *Contributions to Mineralogy and Petrology* 144:206–229.

Lopez-Ramos E. 1975. Geological summary of the Yucatán Peninsula. In *The ocean basins and margins*, edited by Nairn A. and Stehli F. New York: Plenum Press. pp. 257–282.

Osinski G. R. 2003. Impact glasses in fallout suevite from the Ries impact structure, Germany: An analytical SEM study. *Meteoritics & Planetary Science* 38:1641–1667.

Palme H. and Jones A. 2003. Solar system abundances of the elements. In *Treatise on geochemistry,* vol. 1, edited by Davis A. M. Amsterdam: Elsevier. pp. 41–61.

Pilkington M., Ames D. E., and Hildebrand A. R. 2004. Magnetic mineralogy of the Yaxcopoil-1 core, Chicxulub. *Meteoritics & Planetary Science* 39:831–841.

Pope K. O., Ocampo A. C., Fischer A. G., Vega F. J., Ames D. E., King D. T., Jr., Fouke B. W., Wachtman R. J., and Kletetschka G. 2005. Chicxulub impact ejecta deposits in southern Quintana Roo, México, and central Belize. In *Large meteorite impacts III,* edited by Kenkmann T., Hörz, F., and Deutsch A. Boulder, Colorado: Geological Society of America. pp. 171–190.

Potts P. J., Bowles J. F. W., Reed S. J. B., and Cave M. R. 1995. *Microprobe techniques in the earth sciences.* London: Chapman & Hall. 419 p.

Rudnick R. L. and Gao S. 2003. Composition of the continental crust. In *Treatise on geochemistry,* vol. 3, edited by Rudnick R. Amsterdam: Elsevier. pp. 1–64.

Schmitt R. T., Wittmann A., and Stöffler D. 2004. Geochemistry of drill core samples from Yaxcopoil-1, Chicxulub impact crater, Mexico. *Meteoritics & Planetary Science* 39:979–1001.

Schulte P. and Kontny A. 2005. Chicxulub impact ejecta from the Cretaceous-Paleogene (K-P) boundary in northeastern México. In *Large meteorite impacts III,* edited by Kenkmann T., Hörz, F., and Deutsch A. Boulder, Colorado: Geological Society of America. pp. 191–221.

Sharpton V. L., Corrigan C. M., Marin L. E., Urrutia-Fucugauchi J., and Vogel T. A. 1999. Characterization of impact breccias from the Chicxulub impact basin: Implications for excavation and ejecta emplacement (abstract #1515). 30th Lunar and Planetary Science Conference. CD-ROM.

Shukolyukov A. and Lugmair G. W. 1998. Isotopic evidence for the Cretaceous-Tertiary impactor and its type. *Science* 282:927–929.

Stöffler D., Artemieva N. A., Ivanov B. A., Hecht L., Kenkmann T., Schmitt R. T., Tagle R. A., and Wittmann A. 2004. Origin and emplacement of the impact formations at Chicxulub, Mexico, as revealed by the ICDP deep drilling Yaxcopoil-1 and by numerical modeling. *Meteoritics & Planetary Science* 39:1035–1067.

Taylor S. R. and McLennan S. M. 1985. *The continental crust: Its composition and evolution.* Oxford: Blackwell Scientific. 312 p.

Tuchscherer M. G., Reimold W. U., Koeberl C., Gibson R. L., and de Bruin D. 2004a. First petrographic results on impactites from the Yaxcopoil-1 borehole, Chicxulub structure, Mexico. *Meteoritics & Planetary Science* 39:899–930.

Tuchscherer M. G., Reimold W. U., Koeberl C., and Gibson R. L. 2004b. Major and trace element characteristics of impactites from the Yaxcopoil-1 borehole, Chicxulub structure, Mexico. *Meteoritics & Planetary Science* 39:955–978.

Tuchscherer M. G., Reimold W. U., Koeberl C., and Gibson R. L. 2005. Geochemical and petrographic characteristics of impactites and Cretaceous target rocks from the Yaxcopoil-1 borehole, Chicxulub impact structure, Mexico: Implications for target composition. *Meteoritics & Planetary Science* 40:1513–1536.

Utzmann A., Hansteen T. H., and Schmincke H.-U. 2002. Trace element mobility during sub-seafloor alteration of basaltic glass from Ocean Drilling Program site 953 (off Gran Canaria). *International Journal of Earth Sciences* 91:661–679.

Ward W. C., Keller G., Stinnesbeck W., and Adatte T. 1995. Yucatán subsurface stratigraphy: Implications and constraints for the Chicxulub impact. *Geology* 23:873–876.

Wittmann A., Kenkmann T., Schmitt R. T., Hecht L., and Stöffler D. 2004. Impact-related dike breccia lithologies in the ICDP drill core Yaxcopoil-1, Chicxulub impact structure, Mexico. *Meteoritics & Planetary Science* 39:931–954.